Miner Petrol (2017) 111:81–97
DOI 10.1007/s00710-016-0459-x

ORIGINAL PAPER

Multistage amphiboles from the Galinge iron skarn deposit in Qiman Tagh, western China: evidence of igneous rocks replacement

M. Yu[1,2] · C. -Y. Feng[2] · Y. -F. Zhu[1] · J. -W. Mao[2] · Y. -M. Zhao[2] · D. -X. Li[2]

Received: 14 November 2015 / Accepted: 27 July 2016 / Published online: 9 August 2016

Abstract Amphiboles from the Galinge skarn deposit, the largest iron (Fe) polymetallic skarn deposit in the Qiman Tagh metallogenic belt (western China), were formed by multistage fluid-rock interactions. Mineral analysis of the various amphiboles suggest that they were formed by the replacement of mafic to intermediate igneous rocks. The two alteration phases have formed three generations of compositionally distinct amphiboles: Amp-I: Ferro-edenitic hornblende (FE); Amp-II: Deep bluish-green magnesian-hastingsite (MH); Amp-III: Light greenish-beige ferro-actinolite (FA). The Amp-I preserves the primary igneous amphibole composition, and was subsequently replaced by Amp-II. The amphibole Cl content markedly increases from the FE (0.176 − 0.582 wt.%) to the MH (0.894 − 3.161 wt.%), and abruptly drops in the FA (0.017 − 0.039 wt.%). The Cl-rich MH contains the lowest concentration of Si [5.64 − 6.28 atoms per formula unit (apfu)], and the highest (K + Na) values (0.72 − 1.06 apfu) in the amphibole A-site with a high K/(K + Na) of 0.491 to 0.429. Both Mg and Fe contents of the MH and FA vary widely, possibly due to the interactions of magma-derived hydrothermal fluids with the basaltic / andesitic host rocks.

Formation of the Cl-rich MH may have been associated with the early high-temperature and high-saline hydrothermal fluids, meanwhile the Cl-poor FA may have formed from later low-temperature and low-saline hydrothermal fluids. The MH plays an important role for consuming Cl carried by hydrothermal fluids. The Cl-rich fluids may have mobilized some elements, such as Fe, Al, Mg, Ca and Ti from the host rocks. Considerable amounts of Ti, Al, Mg and Fe were incorporated into the sphene and Fe-Ti oxides that coexist with the MH.

Keywords Galinge skarn Fe deposit · Qiman Tagh metallogenic belt · Amphibole · Fe-Ti oxides · Hydrothermal fluids

Editorial handling: G. Hoinkes

✉ C. -Y. Feng
fengchy@cags.ac.cn

[1] School of Earth and Space Sciences, Peking University, Beijing 100871, China

[2] MLR Key Laboratory of Metallogeny and Mineral Assessment, Institute of Mineral Resources, CAGS, No. 26 Baiwanzhuang Street, Xicheng District, Beijing 100037, China

Introduction

The Galinge Fe polymetallic deposit, the largest skarn deposit in the Qiman Tagh metallogenic belt, is located in the contact zone between the Kunlun Mountains and the Qaidam Basin (Fig. 1). The Qiman Tagh metallogenic belt is considered as an high potential porphyry and skarn metallogenic belt, with many deposits indicated to be economic in the past decades, e.g., the Sijiaoyang Pb-Zn skarn, Weibao Pb-Zn-Cu skarn, Yemaquan Fe skarn, Kendekeke Fe skarn, Hutouya Cu polymetallic skarn, Kaerqueka Cu polymetallic skarn, and Ulan Uzhur Cu porphyry deposits (Feng et al. 2011; Mao et al. 2012; Zhao et al. 2013).

Hydrothermal fluids can intensively alter the mineralogy, texture and chemistry of the host rocks. As chemical components are transferred from one geological environment into another, it may promote fluid-mineral reactions as the system moves back toward equilibrium. Evidence of these interactions is common in the residual bulk composition, mineralogy and textures (Baker and Spiegelman 1995; Dutrow et al. 1999). If metasomatism is moderate, clear mineralogical evidence is preserved in the form of skarns or metasomatic minerals. Nevertheless, if alteration effects are very intensive, as a

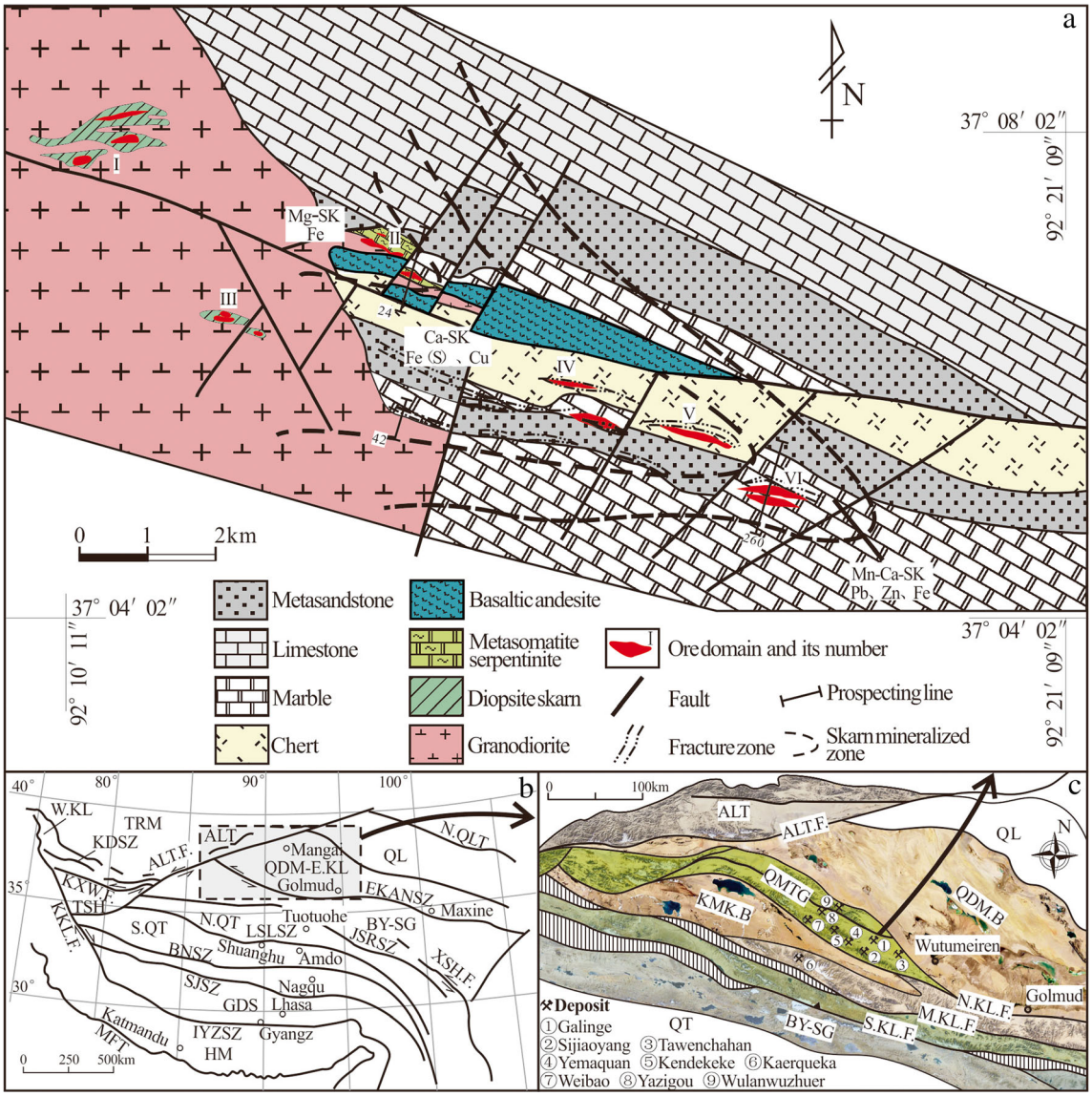

Fig. 1 **a**. Geological map of the Galinge skarn deposit. **b**. Map showing distribution of terranes and suture zones in the Tibet Plateau (Xu et al. 2013). Study area (rectangle) is in the Qiman Tagh orogenic belt. **c**. Geological sketch map of the study area showing orogenic belts and the locations of the skarn deposits. QL: Qilian terrane; QDM-E.KL: Qaidamu-East Kunlun terrane; BY-SG: Bayanhar-Songpan-Ganzi terrane; S.QT: Southern Qiangtang terrane; N.QT: Northern Qiangtang terrane GDS: Gangdise terrane; HM: Himalaya terrane; ALT: Altun terrane; W.KL: West Kunlun terrane; TSH: Tianshuihai terrane; TRM: Tarim terrane; EKANSZ: East Kunlun-Anemaqen suture zone; JSRSZ: Jinsha River suture zone; LSLSZ: Longmuco-Shuanghu-Lancangjiang suture zone; BNSZ: Bangong-Nujiang suture zone; SJSZ: Shenza-Jiali suture zone; IYLZSZ.: Yarlung Zangbo River suture zone; MFT: the main Himalaya thrust fault ALT.F.: Altun fault; S.KL.F.: Southern Kunlun fault; M.KL.F.: Middle Kunlun fault; N.KL.F.: Northern Kunlun fault; N.QLT: the north margin of the Northern Qilian thrust fault; QMTG: Qiman Tagh orogen; ALT: Altun orogen

consequence, only subtle textures and mineralogical features are preserved (Duke 1995). As such, mineralogy and textures of multistage amphiboles may provide important clues of the controlling process of fluid-rock interaction in the Galinge deposit.

This paper reports on an interesting textural and mineralogical feature: Cl-rich amphiboles replacing edenite in the first stage and actinolite replacing amphiboles in the second stage, as observed in the exocontact zone of granodiorite intrusions in the Galinge skarn deposit. Cl-rich amphiboles have been reported in many skarn deposit, e.g., the highest Cl concentrations (7.24 wt.%) were reported from the Dashkesan skarn Fe deposit in Azerbaijan (Krutov 1936); Jacobson (1975) reported Cl-rich calcic amphiboles containing 5.34 and 6.51 wt.% Cl, respectively, from skarn in Dashkesan and mylonite in St. Paul's Rock, and Dick and Robinson (1979) reported Cl-rich calcic amphibole containing 3.09 wt.% Cl from a sphalerite skarn in southern Yukon. The amphibole group is characterized by extensive chemical substitutions and compositionally diverse members. This chemical complexity makes

amphibole a good recorder for the compositional transformation of fluids. Amphibole is also useful for tracking the compositional evolution of igneous and metamorphic rocks, and for fluid infiltration and leaching fingerprinting. Especially, Cl-rich amphiboles shed light on the volatile contributions to mineralization. This study aims to relate the amphibole compositional variation to the chemical / physical variation in the magma-derived hydrothermal fluid stages, and determine the link between amphibole formation and igneous rock replacement.

Regional geology

The Kunlun Mountains are located in the northernmost Tibetan Plateau. The Altun Fault divides the Kunlun Mountain into East- and West Kunlun. Tectonically, East Kunlun is subdivided into four tectonic belts (from north to south), i.e., North Kunlun, Middle Kunlun, South Kunlun, and the Songpan-Garze tectonic belts (Fig. 1) (Li et al. 2001; Luo et al. 1999). The North Kunlun belt, also known as Qiman Tagh fold belt, is characterized by intense deformation, metamorphism and magmatism. WNW-NW-trending reverse / transpressional faults are the major structures in the Qiman Tagh back-arc rift basin; other WNW-trending structures include folds and schistosity planes. At the western end, the fault system turns sharply from NW-trending to SW-trending, subparallel to the Altun Fault in its north. To the east, the Qiman Tagh Thrust fades out into the Qaidam Basin, with its slip transferred to the North Kunlun Thrust (Bally 1986). As for the metamorphic rocks, the Jinshuikou Group metagranites and metasediments (amphibolite-granulite facies) are regarded as the Precambrian metamorphic basement of the Qaidam Basin (Zhang et al. 2003).

The Qiman Tagh fold belt contains a NE-trending and a NW-trending magmatic belt (Fig. 1) (Wu et al. 2011). The NE-trending magmatic belt is dominated by Jurassic and late Silurian-early Devonian igneous rocks, the NW-trending one is mainly composed of the later Triassic igneous rocks (Fig. 1) (Wu et al. 2011). Overall, Qiman Tagh experienced predominantly four magmatic intrusive events, including the Late Proterozoic, Cambrian - Early Devonian, Late Carboniferous, and Triassic events. The Triassic period is the most important period for the evolution of Qiman Tagh (Feng et al. 2012; Wang et al. 2009). Then, the region was in a post-collisional, compressive to extension transitional tectonic regime, as shown by the voluminous development of calc-alkaline and alkaline granitoids (Feng et al. 2012; Luo et al. 2002; Yu et al. 2015b). Feng et al. (2012) summarized that the emplacement of post-collisional granitoids occurred mainly during the Late Triassic (ca. 237 − 204 Ma). Many studies suggest that porphyry-skarn mineralization in the Qiman Tagh metallogenic belt is closely related to the Late Triassic calc-alkaline and alkaline intermediate-felsic intrusions (Feng et al. 2010; Mao et al. 2012; Zhao et al. 2013).

Ore deposit geology

The Galinge skarn Fe polymetallic deposit is, from west to east, divided into six ore domains (Fig. 1). The I and III ore domains are situated within blocks of wall rocks surrounded by the granodiorite intrusion, and the ore bodies predominately occur in garnet and diopside skarn rocks; the II ore domain is located at the contact zone between the granodiorite and dolomitic marble, and the ore bodies mainly occur in magnesian skarn rocks; the IV, V and VI ore domains are distributed along a WNW-trending fracture zone within the exocontact zone, and the ore bodies occur in calcic skarns and altered basaltic andesite rocks. This study focuses on the altered basaltic andesite rocks in the IV, V and VI ore domains.

Skarn development at Galinge can be divided into prograde- and retrograde skarn stages. The prograde alteration was extensive, and generated garnet, pyroxene, wollastonite, forsterite, hortonolite and chondrodite. The retrograde alteration yielded abundant gangue minerals, including epidote, magnesian-hastingsite, ferro-actinolite, tourmaline, axinite, chlorite, phlogopite, serpentine and sphene, as well as ore minerals such as magnetite, ilmenite, chalcopyrite, galena and sphalerite. During the sulfide stage mainly low-temperature minerals developed, e.g., calcite, fluorite, pyrrhotite and pyrite.

Based on the mineral assemblages, the Galinge deposit can be roughly divided into three proximal to distal skarn zones; i.e. the magnesian skarn (Mg-SK), the calcium-magnesian skarn (Ca-Mg-SK) and the manganese-calcium skarn (Mn-Ca-SK) zones (Fig. 1) (Yu et al. 2013a). The Mg-SK is developed in the II ore domain, and is featured by the widespread occurrence of Mg-rich minerals, including forsterite, hortonolite, serpentine, Mg-chlorite, chondrodite and phlogopite. The Ca-Mg-SK, occurring in the IV and V ore domains, is associated with the metamorphism of mafic volcanic rocks and marbles, and is characterized by garnet, pyroxene, tourmaline, axinite, magnesian-hastingsite, ferro-actinolite and epidote. The distal Mn-Ca-SK zone of the VI ore domain contains johannsenite, galena and sphalerite.

The basaltic andesites from the Cambrian-Ordovician lower Tanjianshan Formation are widespread and interbeded with the sedimentary rocks. Fresh basaltic andesite at Galinge is composed of plagioclase (65 to 75%), pyroxene (10 to 15%), amphibole (10 to 15%) and biotite (5 to 10%) (Fig. 2). Accessory minerals include magnetite, ilmenite, apatite, zircon and sphene. Some euhedral plagioclase phenocrysts (An_{38-47}) have rims with higher An contents (An_{61-66}). Pyroxene, mainly composed of augite, occurs as corroded crystals with its margins altered to amphibole. Abundant igneous amphiboles show edenitic composition, and are

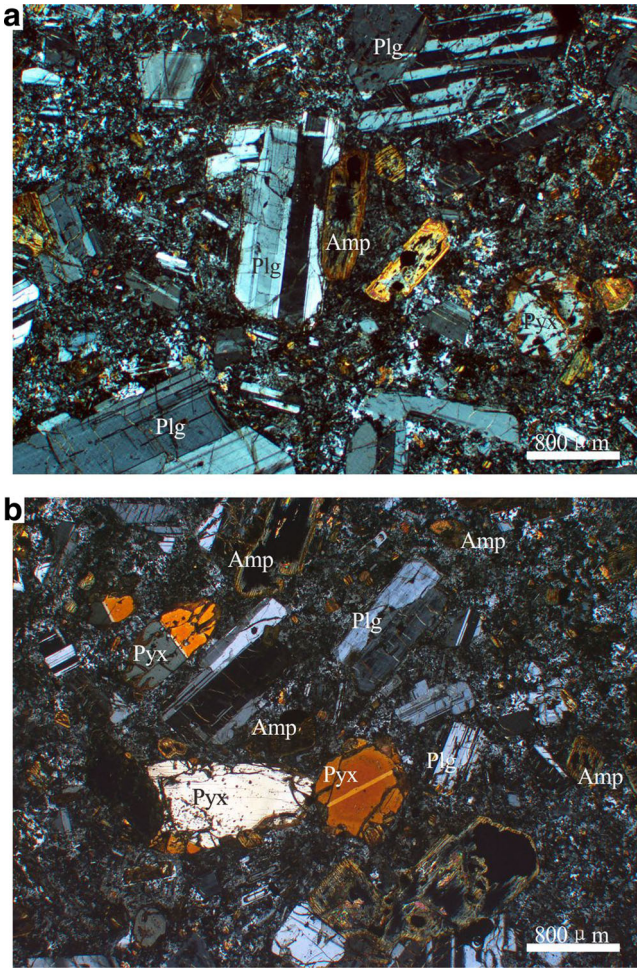

Fig. 2 Photomicrographs of the porphyritic basaltic andesite at Galinge mainly showing the phenocryst of plagioclase, pyroxene and amphibole. Amp-amphibole; Plg-plagioclase; Pyx-pyroxene; crossed polars

partially altered to chlorite with biotite. Magnetite mainly occurs as disseminated anhedral grains in the groundmass, and always comprises polymineralic grains with trellis- or composite-type magnetite-ilmenite intergrowths as a consequence of oxyexsolution of titaniferous magnetite.

The Triassic Galinge granodiorite (229.51 ± 0.6 Ma) (Yu 2013), intruding into the Cambrian to Ordovician Qiman Tagh strata, is metaluminous and calc-alkaline (Yu 2013). Major minerals include plagioclase (35 to 60%), K-feldspar (5 to 35%), quartz (5 to 40%), hornblende, biotite ± clinopyroxene ± sphene ± apatite ± opaques. Plagioclase and K-feldspar are subhedral to euhedral, and amphibole and biotite are subhedral. Quartz occurs as an irregularly-shaped interstitial phase. The rocks are commonly altered: Relict clinopyroxenes occur as corroded crystals with its margins altered to amphibole. Biotite is partly altered to chlorite. Interstitial quartz has abundant fluid inclusions containing solid phases. The Fe-Pb-Zn-Cu mineralization is considered to be related to Galinge granodiorite. Metallogenic age was estimated on dating the ore-bearing phlogopite skarn rocks using ^{40}Ar-^{39}Ar dating method, which yielded an isochron age of 234.1 ± 3Ma, and a plateau age of 235.8 ± 1.7 Ma (*Yu et al.* 2015a).

Petrography

The Galinge multistage amphiboles are predominantly associated with altered basaltic andesite (Fig. 3). Specimens studied in detail shows a clear and variable degree of replacement between the infiltrating fluids and the basaltic andesite along the replacement direction (Fig. 3a). In the less altered parts, phenocrysts of plagioclase and amphibole are well preserved; in the moderately altered parts (outer shell about 3 cm wide) (Fig. 3b), only plagioclase phenocrysts are preserved, whilst the amphibole phenocrysts and groundmass are completely altered to elongated secondary amphibole aggregates. In the intensively altered parts (inner shell) (Fig. 3b), the basaltic andesite rock was completely altered to a rock composed of greenish yellow garnets and dark green amphiboles, a few garnet grains from pseudomorphs replacing elongated feldspars.

Amphiboles in the altered basaltic andesite can be petrographically and compositionally divided into three types, i.e., Amp-I, Amp-II and Amp-III (Figs. 4 and 5). Under the microscope, Amp-II (Gen-2: Generation 2) formed after Amp-I (Gen-1: Generation 1) (Fig. 4a–c), as supported by the distinctive replacement of Amp-I by Amp-II. Amp-II, in turn, is partially replaced by Amp-III (Gen-3: Generation 3) (Fig. 4d–f). Optical and back-scattered electron (BSE) imaging show similar complex textures of the three amphibole generations (Fig. 5).

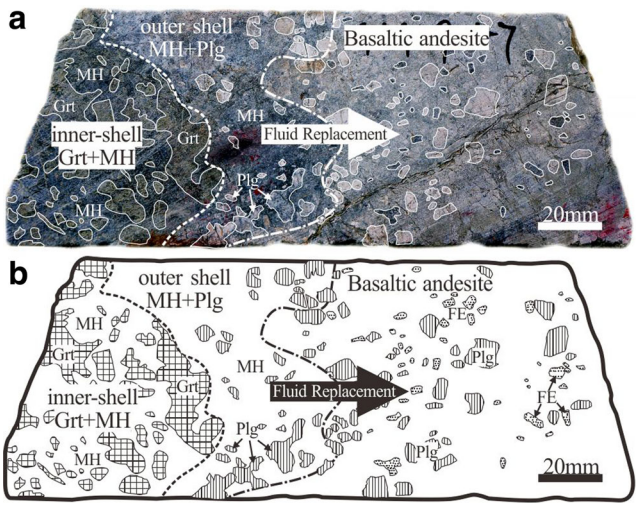

Fig. 3 **a**, **b** Photograph and sketch showing the reaction front in a hand specimen. The inner shell contains an assemblage of garnet and amphibole, and the outer shell develops only amphibole. The arrow shows the fluid replacement direction. Grt-garnet; MH-magnesian hastingsite; FE-ferro edenite

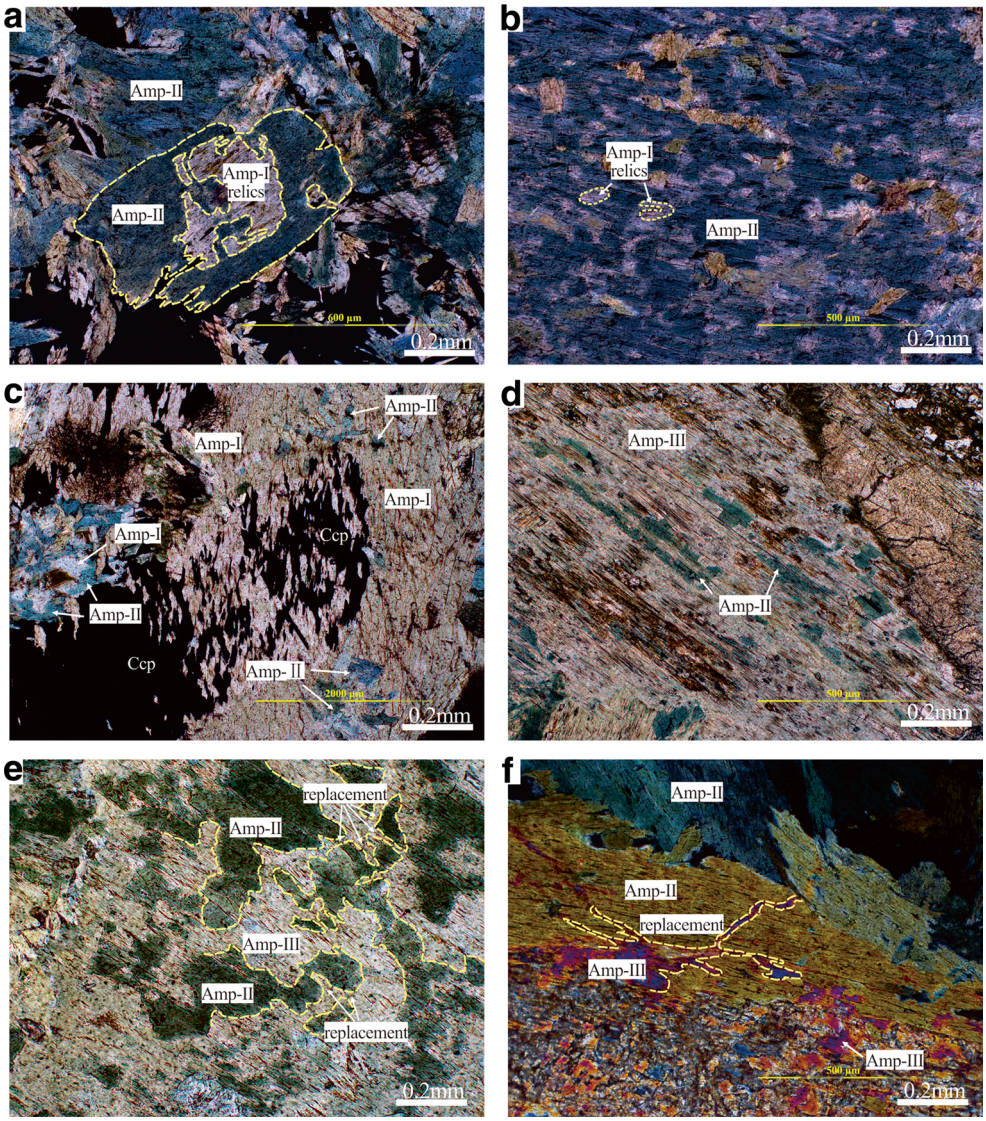

Fig. 4 Photomicrographs of the three amphibole generations. **a** Zoned grains of amphibole with relics of brown cores (Amp-I) and bluish-green rims (Amp-II), plane polarized light. **b** Fibrous amphibole displaying the texture of the host brown Amp-I and the bluish-green Amp-II growth in the fibers as observed in sections cut parallel to the fiber length, plane polarized light. **c** Amp-II (and ore minerals) replacing Amp-I along the rhombic cleavages, plane polarized light. **d** Host Amp-II being replaced by Amp-III, plane polarized light. **e** Host Amp-II and Amp-III fiber growth, plane polarized light. **f** Amp-III in a dendritic aggregate vein cutting Amp-II grains, cross-polarized light

Amp-I

The earliest Amp-I may have preserved the primary igneous edenitic composition of the basaltic andesite, and it coexists with plagioclase phenocrysts in the least altered rocks. Subsequently, it was replaced by Amp-II and occurring as pseudomorphs. Cores of brown amphibole (Amp-I) are rimmed and partly to nearly totally replaced by bluish green amphibole (Amp-II) (Fig. 4a). In some places, ore minerals (± Amp-II) replaced Amp-I along the rhombic cleavages (Fig. 4c).

Amp-II

Amp-II is the major constituent of the ore-bearing skarn from the Ca-SK zones, and was mainly associated with moderately to extensively altered basaltic andesite. In moderately altered rocks, Amp-II coexists with anhedral plagioclase phenocryst, which occur as fine grained aggregates in the groundmass. In addition, Amp-II always occurs as prismatic bluish green crystals up to 1cm long in interstices of very coarse-grained and strongly birefringent grossular-andradite in extensively altered basaltic andesite (Fig. 3). Some Amp-II crystals locally show concentric oscillatory zonation. Amp-II generally coexists with garnets, magnetite, chalcopyrite, pyrrhotite, pyrite, and some plagioclase with in larger garnet pseudomorphs. Amp-II also occurs in garnet-free skarn rocks; in this case the coexisting accessory minerals include apatite, sphene, actinolite, magnetite, pyrite, pyrrhotite and chalcopyrite. Back-scattered electron (BSE) imaging of the sphene (Fig. 6) shows that it contains a light grey core and a dark grey rim, which suggests that the growth of sphene may have occurred in two stages. Besides, abundant sphene was also found coexisting with magnesian-hastingsite. Magnetite-ilmenite exsolutions were locally observed in their skarn rocks.

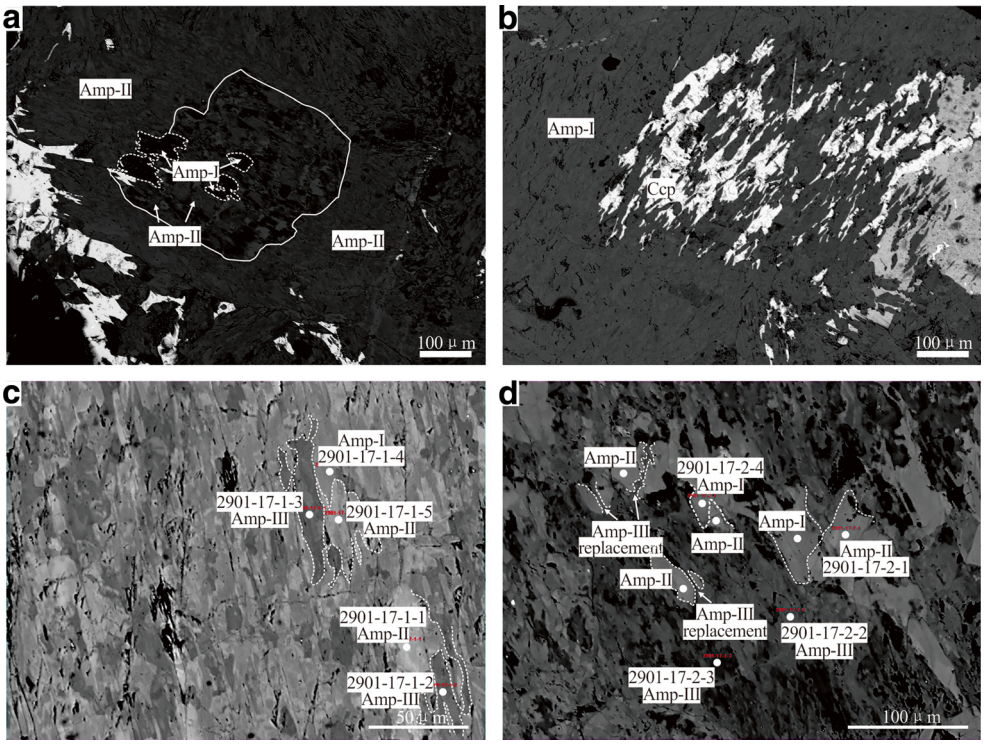

Fig. 5 BSE images of amphiboles from the Galinge skarn deposit. The figures **a** – **d** clearly show the replacement relationships, and Amp-I to Amp-III show grey scales. The numbered points show the electron microprobe analyses spots

Amp-III

The light green Amp-III (actinolite), is common in the Galinge skarn deposit. Bluish-green Amp-II is clearly crosscut and replaced by the Amp-III (Fig. 4d, e). Besides, Amp-III in dendritic veins crosscut Amp-II grains. In some places, Amp-III aggregates occur together with the Amp-II (Fig. 4f).

Analytical method

Electron-microprobe analyses of amphibole were conducted with wavelength-dispersive spectrometry (WDS) using a JOEL JXA-823V Electron Probe Micro Analyzer (EPMA) at the MLR Key Laboratory of Metallogeny and Mineral Assessment, Institute of Mineral Resources, Chinese Academy of Geological Sciences (Beijing) China. Analytical conditions were: accelerating potential 15 kV, beam current 5-10 nA, 3-5μm focused electron beam. The analyses were calibrated using jadeite (Si, Na, and Al), forsterite (Mg), orthoclase (K), apatite (P), wollastonite (Ca), rutile (Ti), halite (Cl), and synthetic oxide (Cr, Mn, Fe, Ni) as standards.

In order to calculate the stoichiometry of the amphiboles and estimate the amounts of H_2O, several assumptions were made. The general formula of amphiboles can be expressed as $W_{0\text{-}1}X_2Y_5Z_8O_{22}(OH,O,F)_2$, where W represents cations occupying the A-site; X and Y are octahedrally coordinated cations occupying the M4 and M1-M3 positions, respectively. Z represents tetrahedrally coordinated small cations in the T-site. The calculation of amphibole formulae was based on a total cation charge of 46 (*i.e.* ∑O=22; ∑OH, Cl=2), and was determined on the assumption that Si + Al + Ti + Fe + Mg + Ca = 15 (15eNK: $Si + Al^{IV}=8$; Al^{VI} + Ti + Fe + Mg + Ca = 7); Concentration of H_2O was calculated assuming ∑O3 = 2.0 (OH, F, Cl) apfu.

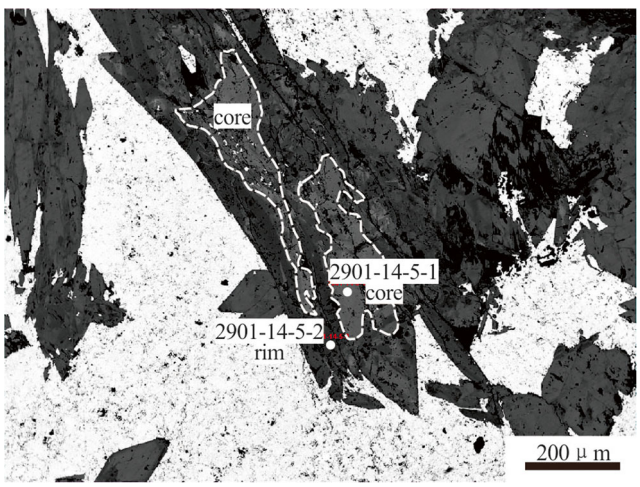

Fig. 6 BSE images of sphene, showing light grey cores and dark grey rims. The numbered points show the electron microprobe analyses spots

Mineral composition

The chemical composition of amphibole group minerals is very complex, and thus the problems inherent in the classification of such a group of minerals are obvious. Currently, two classification schemes are largely used: the first one is based

on the cations A, M4 and T sites (Fig. 7a) (Leake 1978; Leake et al. 1997, 2004); the second one is based on the cations A, M4 and M1-M3 sites of the amphibole structure (Fig. 7b) (Hawthorne and Oberti 2006). Both classification schemes highlight the compositional changes from Amp-I to Amp-III.

The Galinge amphiboles show a considerable variation with respect to $Mg^{2+}/(Fe^{2+} + Mg)$ and Si (apfu) (Fig. 7a) (Leake et al. 2004). The igneous Amp-I shows ferro-edenitic hornblende (FE) composition. Amp-II is magnesian-hastingsite (MH); Amp-III is ferro-actinolite (FA). The Si content ranges widely from the MH to the FA. The MH has the lowest Si content (5.635 − 6.278 apfu), followed by FE (6.505 − 6.817 apfu), and FA having the highest Si content (7.383 − 7.851 apfu) (Table 1). However, almost all X_{Mg} (X_{Mg} = Mg/ (Fe^{2+} + Mg)) values are below 0.5 (Table 1, Fig. 7a). In the Fig. 7b, Na_A (apfu) vs. $(Al+Fe^{3+}+2Ti)_C$ (apfu) (Hawthorne et al. 2012), the Na content increases with $(Al+Fe^{3+}+2Ti)_C$. The Amp-II has the highest Na content (0.333 – 0.490 apfu), followed by FE (0.267 – 0.35 apfu), whereas the FA has the lowest Na content (0.03 – 0.162 apfu) (Table 1, Fig. 7b).

In the Ca-Fe^{2+}-Mg ternary diagram (Fig. 8), the distinct compositions can be distinguished for amphiboles from different generations. The Fe and Mg contents vary largely among the different amphibole generations. In addition, the Ca contents clearly distinguish Amp-I, Amp-II and Amp-III, e.g., the Ca content increases from Amp-I to Amp-II, and then decreases from Amp-II to Amp-III.

In Figure 9a, (Na + K) values (apfu) in the A-site are plotted against Si in the tetrahedral site, showing a strongly negative correlation for all amphibole generations. The (Na + K) values are markedly higher in Amp-II MH (0.721 − 7.851 apfu), when compared to the Amp-I FE (0.487 − 0.649 apfu), but much lower in the Amp-III FA (0.034 − 0.281 apfu).

The three amphibole types Amp-I, Amp-II and Amp-III contain 0.582 − 0.176, 3.161 − 0.894 and 0.039 − 0.017 wt.% Cl, respectively (Fig. 10a, b). In Fig. 10a, the mole fraction of K in the A- site (X_K = K/ (K + Na)) vs. X_{Cl} (X_{Cl}= Cl/ (Cl + OH)) shows extensive positive correlation for Amp-II and Amp-III. Amp-II has elevated X_K (0.491 − 0.629) and X_{Cl} (0.118 − 0.439); whereas, Amp-III has low X_K (0.129 − 0.481) and X_{Cl} (0.002 − 0.006). In contrast, Amp-I shows no obvious correlation between X_{Cl} and X_K. Moreover, the mole fraction of Al vs. X_{Cl} shows similar correlations (Fig. 10b).

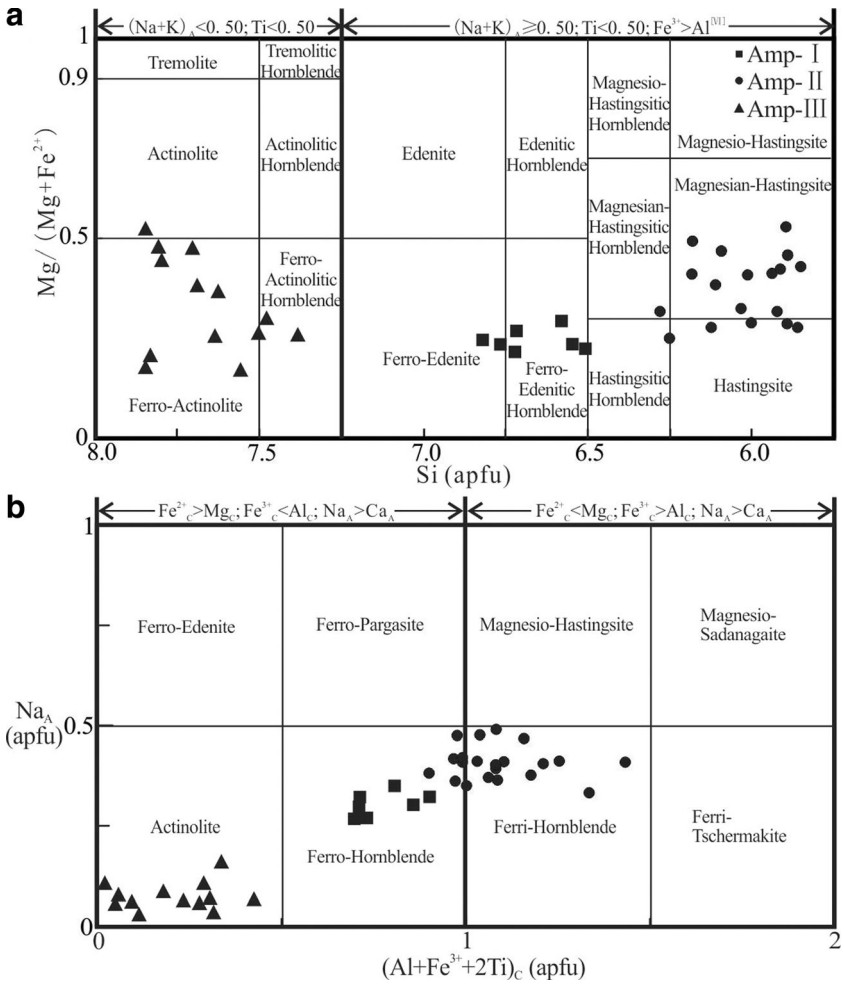

Fig. 7 **a** Amphibole classification diagram (Leake 1978). Amphiboles from the Galinge skarn deposit vary in composition from Amp-I to Amp-III, i.e., ferro-edenite (FE) → magnesian hastingsite (MH) → ferro-actinolite (FA). **b** Compositional variations from Amp-I to Amp-III based on Na_A (apfu) content and $(Al+Fe^{3+}+2Ti)_C$ (apfu) content (Hawthorne et al. 2012)

Table 1 Representative electron microprobe analysis of Amp-I, Amp-II and Amp-III from the Galinge skarn deposit

	Amp-I			Amp-II						Amp-III					
Sample	2901-17-2-4	Average (7)	R	2901-11	Average (6)	R	21605-87	Average (15)	R	2901-12-1-2	Average (8)	R	4204-15-1.3	Average (4)	R
Name	FE	FE		MH	MH		MH	MH		FA	FA		FA	FA	
Ore domain	II	II		II	II		V	V		II	II		IV	IV	
SiO_2	42.69	42.19	0.66	38.35	38.88	0.61	36.05	36.81	1.22	50.66	50.22	1.68	49.13	49.68	1.15
TiO_2	0.00	0.11	0.06	0.10	0.11	0.05	0.33	0.33	0.16	0.02	0.04	0.04	0.00	0.03	0.02
Al_2O_3	8.01	8.72	0.77	12.15	11.59	0.67	14.56	12.87	1.08	1.19	2.56	1.20	3.36	2.10	1.02
FeO	28.34	27.97	0.54	24.20	24.78	2.48	23.13	23.09	2.45	21.37	23.09	3.01	28.72	30.31	0.95
MnO	0.51	0.45	0.08	0.37	0.39	0.08	0.30	0.25	0.05	0.40	0.89	0.59	0.23	0.37	0.11
MgO	4.28	4.42	0.42	8.67	6.39	1.49	5.68	6.21	1.31	9.79	8.16	2.28	5.58	4.37	0.85
CaO	11.56	11.57	0.14	11.46	11.81	0.29	12.13	11.83	0.35	11.73	11.97	0.34	11.84	11.86	0.37
Na_2O	0.88	0.99	0.09	1.12	1.28	0.15	1.31	1.33	0.13	0.36	0.25	0.13	0.37	0.26	0.07
K_2O	1.17	1.28	0.12	2.24	2.13	0.23	3.13	2.73	0.29	0.38	0.20	0.17	0.50	0.33	0.11
F	0.23	0.10	0.14	0.00	0.01	0.02	0.04	0.11	0.08	0.00	0.09	0.11	0.11	0.15	0.03
Cl	0.42	0.39	0.15	1.08	1.20	0.23	1.90	1.91	0.62	0.03	0.02	0.01	0.04	0.04	0.01
H_2O	1.66	1.75	0.07	1.68	1.59	0.08	1.38	1.32	0.16	1.94	1.91	0.08	1.89	1.85	0.03
Total	98.09	98.18	0.47	101.41	98.86	1.76	99.94	98.80	1.07	95.92	97.50	0.92	99.88	99.50	1.01
Si	6.763	6.664	0.111	5.894	6.120	0.132	5.749	5.922	0.144	7.798	7.665	0.146	7.507	7.683	0.152
$^{[4]}Al$	1.237	1.336	0.111	2.106	1.880	0.132	2.251	2.078	0.144	0.202	0.335	0.146	0.493	0.317	0.152
∑T	8.000	8.000	0.000	8.000	8.000	0.000	8.000	8.000	0.000	8.000	8.000	0.000	8.000	8.000	0.000
$^{[6]}Al$	0.258	0.287	0.044	0.095	0.270	0.109	0.481	0.359	0.133	0.014	0.128	0.081	0.112	0.066	0.034
Ti	0.000	0.013	0.007	0.012	0.013	0.005	0.040	0.040	0.019	0.002	0.004	0.005	0.000	0.004	0.003
Fe^{3+}	0.472	0.461	0.067	1.215	0.766	0.216	0.649	0.663	0.187	0.001	0.084	0.072	0.176	0.101	0.093
Fe^{2+}	3.228	3.180	0.128	1.757	2.409	0.427	2.359	2.368	0.308	2.749	2.860	0.390	3.474	3.809	0.224
Mn	0.069	0.061	0.011	0.048	0.053	0.011	0.040	0.034	0.008	0.052	0.115	0.077	0.030	0.049	0.014
Mg	1.011	1.041	0.096	1.987	1.497	0.334	1.359	1.494	0.300	2.247	1.851	0.494	1.271	1.005	0.183
Ca	1.962	1.957	0.021	1.886	1.992	0.055	2.073	2.041	0.062	1.934	1.958	0.042	1.938	1.966	0.076
∑M1,2,3	7.000	7.000	0.000	7.000	7.000	0.000	7.000	7.000	0.000	7.000	7.000	0.000	7.000	7.000	0.000
$^{[A]}Na$	0.270	0.304	0.028	0.333	0.390	0.048	0.405	0.413	0.037	0.108	0.075	0.038	0.108	0.079	0.019
K	0.237	0.259	0.024	0.439	0.427	0.046	0.636	0.562	0.066	0.074	0.039	0.034	0.097	0.064	0.021
∑A	0.507	0.563	0.050	0.772	0.817	0.086	1.041	0.975	0.075	0.182	0.115	0.070	0.206	0.143	0.038
F	0.129	0.054	0.077	0.000	0.005	0.010	0.020	0.061	0.046	0.000	0.051	0.061	0.060	0.084	0.017
Cl	0.113	0.105	0.039	0.281	0.321	0.063	0.511	0.521	0.178	0.007	0.006	0.002	0.010	0.009	0.002
OH	1.758	1.842	0.070	1.719	1.674	0.071	1.469	1.418	0.153	1.993	1.943	0.062	1.930	1.906	0.016
∑O3	2.000	2.000	0.000	2.000	2.000	0.000	2.000	2.000	0.000	2.000	2.000	0.000	2.000	2.000	0.000
X_{Mg}	0.238	0.247	0.024	0.531	0.386	0.095	0.366	0.387	0.078	0.450	0.391	0.096	0.268	0.209	0.038
X_{Cl}	0.060	0.054	0.019	0.141	0.161	0.032	0.258	0.267	0.087	0.004	0.003	0.001	0.005	0.005	0.001
X_K	0.468	0.459	0.012	0.569	0.523	0.025	0.611	0.575	0.036	0.408	0.307	0.093	0.473	0.443	0.042
X_{Al}	0.155	0.167	0.014	0.263	0.235	0.017	0.281	0.260	0.018	0.025	0.042	0.018	0.062	0.040	0.019

FE:ferro-edenite; MH: magnesian-hastingsite; FA: ferro-actinolite;

The general formulae of amphiboles: $W_{0\text{-}1}X_2Y_5Z_8O_{22}$ (OH, O, F)$_2$;

The structural formulae calculation based on 15eNK: Si + $^{[4]}$Al=8; $^{[6]}$Al + Ti + Fe + Mg + Ca = 7);

*X*Mg = Mg/(Mg + Fe^{2+}); *X*Cl = Cl/(Cl + OH^-); *X*K = K/ (K + Na); *X*Al = Al/ (Al +Si);

The formulae of MH: $(Na, K)_{0.930}(Ca, Mg, Mn, Fe^{2+})_{5.941}(Fe^{3+}, Al, Ti)_{1.059}(Al, Si)_8O_{22}(F, Cl, OH)_2$

The formulae of FE: $(Na, K)_{0.563}(Ca, Mg, Mn, Fe2+)_{6.239}(Fe3+, Al, Ti)_{0.761}(Al, Si)_8O_{22}(F, Cl, OH)_2$

The formulae of FA: $(Na, K)_{0.123}(Ca, Mg, Mn, Fe2+)_{6.798}(Fe3+, Al, Ti)_{0.202}(Al, Si)_8O_{22}(F, Cl, OH)_2$

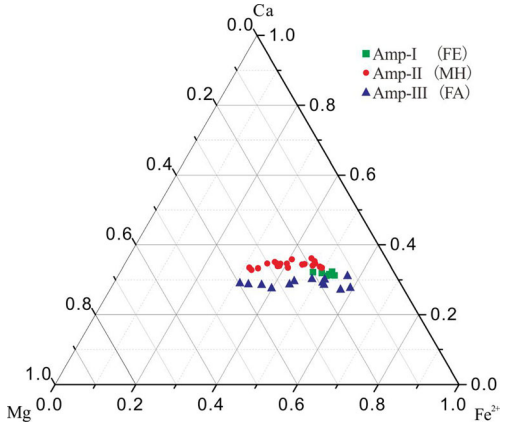

Fig. 8 Triangular Ca-Fe-Mg plot (in total molar proportions) for Amp-I, Amp-II and Amp-III from the Galinge skarn deposit

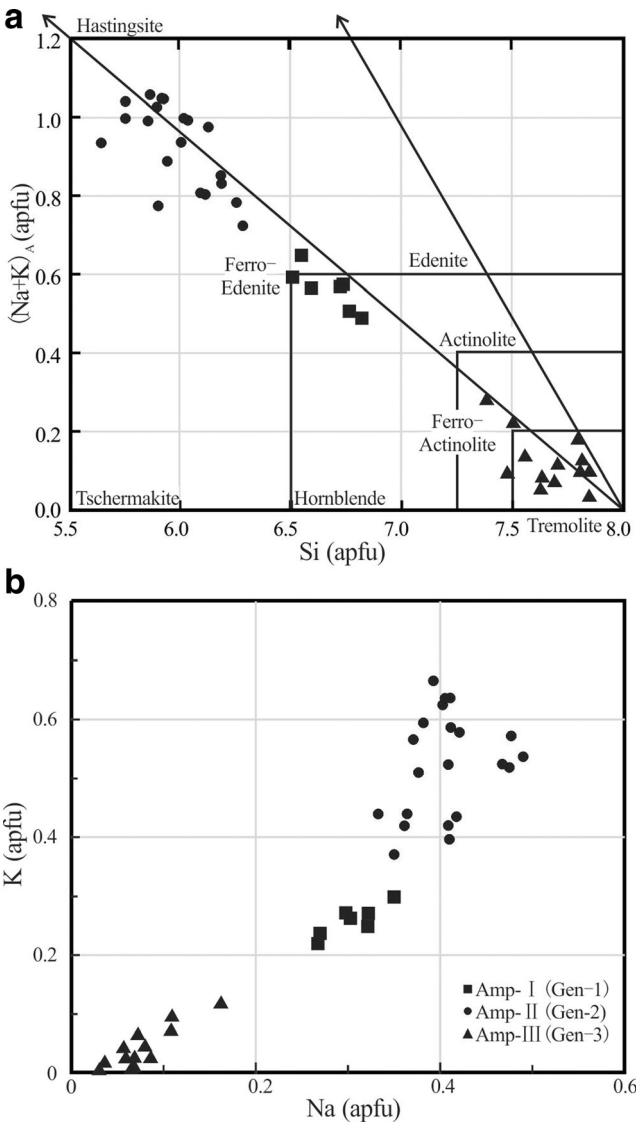

Fig. 9 **a** Plot of (Na+K) vs. Si of the amphiboles from Galinge skarn deposit. **b** Plot of K vs. Na of the amphiboles from Galinge skarn deposit

The chemical compositions of Fe-Ti oxides in the skarn and igneous rocks were also analyzed (Table 2). Grigsby (1990) found that TiO_2, Cr_2O_3, MnO, MgO, V_2O_3 and Al_2O_3 contents of magnetite could discriminate igneous magnetite from hydrothermal one. In the Mg-(Mn+Zn)-(V+Cr+Al) ternary diagram (Fig. 11), the magnetite-ilmenite assemblage from the basaltic andesite contains distinctively higher $V_2O_3 + Cr_2O_3 + Al_2O_3$, and lower MgO and MnO + ZnO than the magnetite-ilmenite assemblage from the skarns. Our data show that Al and Ti are on average considerably more concentrated in igneous magnetite (2.36 wt.% Al_2O_3 and 8.51 wt.% TiO_2) than in hydrothermal one (0.87 wt.% Al_2O_3 and 1.27 wt.% TiO_2) (Table 2).

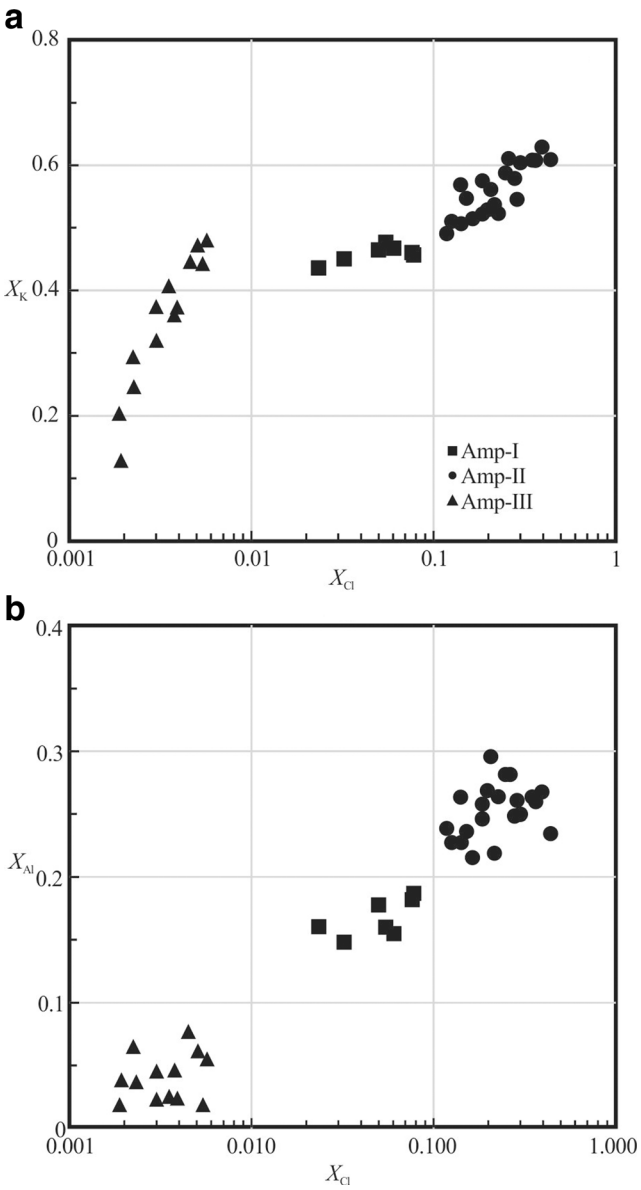

Fig. 10 **a** Plot of X_K vs. X_{Cl} of Amp-1 to Amp-3 amphiboles. The X_{Cl} values show strong linear correlations with the X_K values. **b** Plot of X_{Al} vs. X_{Cl} of Amp-I to Amp-III amphiboles. The X_{Cl} values show linear correlations with the X_K values

Table 2 Mineral chemical compositions of coexisting magnetite-ilmenite pairs from the fresh mafic volcanic rocks and skarn wall rocks

	Igneous ilmenite–magnetite						Hydrothermal ilmenite–magnetite									
Comment	38401-2-1-5-4	38401-2-1-5-5	38401-2-1-5-2	38401-2-1-5-3	38401-2-1-1	38401-2-1-5-1	4208-6-4-2	4208-6-4-1	4208-6-4-4	4208-6-4-3	4208-6-4-6	4208-6-4-5	4208-6-4-8	4208-6-4-7	4208-6-4-10	4208-6-4-9
SiO_2	0.24	0.07	0.06	0.00	1.27	0.00	0.03	0.02	0.01	0.02	0.06	0.07	0.03	0.02	0.01	0.03
TiO_2	9.19	48.28	8.23	49.29	8.12	50.06	1.76	49.62	2.24	49.92	0.97	50.09	0.55	50.44	0.86	50.57
$Al2O_3$	2.57	0.12	2.75	0.11	1.78	0.07	1.20	0.03	2.21	0.08	0.29	0.02	0.32	0.02	0.35	0.02
FeO	76.99	47.78	78.79	47.42	78.61	48.65	89.35	24.57	86.18	25.09	91.78	22.95	92.07	24.41	91.30	24.23
MnO	0.64	2.58	0.65	2.32	0.60	2.13	0.65	21.48	0.54	20.19	0.26	20.29	0.28	20.34	0.26	20.21
MgO	0.06	0.09	0.05	0.06	0.07	0.05	0.29	2.75	0.55	3.60	0.26	5.09	0.28	2.71	0.29	4.04
CaO	0.00	0.00	0.00	0.00	0.00	0.00	0.00	0.00	0.00	0.00	0.00	0.00	0.00	0.00	0.00	0.00
Na_2O	0.02	0.03	0.06	0.00	0.06	0.01	0.00	0.01	0.02	0.01	0.01	0.00	0.00	0.00	0.01	0.01
K_2O	0.00	0.02	0.00	0.01	0.00	0.00	0.00	0.00	0.00	0.00	0.00	0.01	0.00	0.00	0.01	0.01
Cr_2O_3	0.03	0.02	0.00	0.00	0.07	0.00	0.10	0.07	0.08	0.05	0.05	0.04	0.11	0.04	0.05	0.00
P_2O_5	0.01	0.00	0.02	0.00	0.03	0.02	0.00	0.00	0.00	0.00	0.00	0.02	0.00	0.01	0.00	0.01
ZnO	0.20	0.00	0.18	0.20	0.29	0.00	0.34	0.13	0.45	0.10	0.17	0.11	0.11	0.13	0.05	0.01
$V2O_3$	0.75	0.67	0.66	0.68	0.94	0.78	0.16	0.21	0.08	0.24	0.13	0.34	0.07	0.31	0.11	0.23
NiO	0.00	0.00	0.02	0.00	0.00	0.00	0.02	0.00	0.00	0.00	0.00	0.00	0.03	0.00	0.00	0.00
Total	90.69	99.66	91.45	100.09	91.82	101.78	94.03	98.91	92.47	99.38	94.02	99.05	93.96	98.43	93.37	99.36
Name	Ma	Ilm	Ma	Ilm	Ma	Ilm	Ma	Ilm	Ma	Ilm	Ma	Ilm	Ma	Ilm	Ma	Ilm
	xusp	*xilm*	*xusp*	*xilm*	*xusp*	*xilm*	*xusp*	*xilm*	*xusp*	*xilm*	*xusp*	*xilm*	*xusp*	*xilm*	*xusp*	*xilm*
	0.29	0.92	0.26	0.94	0.25	0.94	0.05	0.87	0.07	0.87	0.03	0.87	0.02	0.92	0.02	0.89
T/°C	740.26		686.18		690.73		674.05		688.94		646.42		581.8		628.22	
lnfO_2	–15.44		–17.30		–17.09		–14.96		–14.74		–15.20		–17.94		–15.99	

The Fe-Ti oxides geothermometer and oxygen barometer were calculated based on ILMAT (Lepage 2003)

The chemical compositions of the sphene coexisting with Amp-II are listed in Table 3. They show high CaO (27.62 − 28.96 wt.%), Al_2O_3 (2.72 − 4.62 wt.%) and F (0.4 − 0.9 wt.%). The TiO_2 and Al_2O_3 in the second stage rims (average: TiO_2 = 32.29 wt.%, Al_2O_3 = 3.35 wt.%) are significantly higher than in the first stage cores (average: TiO_2 = 28.16 wt.%, Al_2O_3 = 3.17 wt.%).

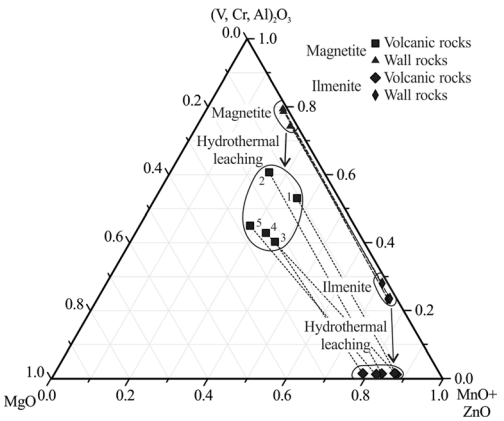

Fig. 11 MgO-(MnO+ZnO)-($(V,Cr,Al)_2O_3$) ternary diagram of the coexisting Fe-Ti oxides from the fresh volcanic rocks and skarn wall rocks. From the volcanic rocks to wall rocks, the MgO and (MnO + ZnO) contents of magnetite and ilmenite increase, and the V_2O_3 + Cr_2O_3 + Al_2O_3 contents decrease

Fluid inclusions

Fresh and altered granodiorite samples which are in contact with the ore body were used for fluid inclusion thermometry. Fluid inclusion in different generations of quartz were analyzed. They reflect entrapment of fluids during different PTX conditions. Primary inclusions in igneous quartz reflects the properties of the early magmatic fluid, inclusions in later formed quartz reflect the interaction between the residual fluid and the pluton, and the inclusions in the skarn minerals allows to constrain the PTX conditions of the hydrothermal fluids.

In skarn mineral phases, the composition is consistently correlated with fluid inclusion salinity and temperature. Fluid inclusions are particularly useful in documenting the temporal and spatial evolution of skarn-forming fluids, and provide evidence for the temperature and salinity shifts between prograde- and retrograde alteration. For example, fluid inclusions of prograde skarn minerals have homogenization temperatures above 300°C, and salinities up to 50 wt. % NaCl equivalent; whereas, inclusions in the retrograde stage have homogenization temperatures up to 250°C, and salinities up to

Table 3 Mineral chemical composition of sphene coexisting with the magnesian hastingsite

Comment	2901-14-7-1	2901-14-7-2	2901-14-7-3	2901-14-7-4	2901-14-5-1(core)	2901-14-5-2(rim)	2901-14-6-2(core)	2901-14-6-1(rim)
SiO_2	30.85	29.41	31.50	30.83	30.12	31.48	30.94	31.00
TiO_2	28.54	29.69	29.29	30.87	27.93	32.03	28.40	32.56
Al_2O_3	3.65	3.69	4.63	2.72	3.37	3.58	2.97	3.13
FeO	0.53	0.75	0.98	0.82	0.63	0.43	0.95	0.60
MnO	0.00	0.00	0.03	0.04	0.00	0.02	0.02	0.02
MgO	0.01	0.04	0.03	0.01	0.00	0.01	0.00	0.00
CaO	28.41	27.62	28.63	28.27	27.68	28.94	28.24	28.96
Na_2O	0.01	0.02	0.00	0.00	0.04	0.00	0.00	0.03
K_2O	0.00	0.00	0.00	0.00	0.00	0.00	0.00	0.00
P_2O_5	0.02	0.05	0.02	0.00	0.00	0.00	0.00	0.00
V_2O_3	0.16	0.22	0.19	0.10	0.18	0.24	0.27	0.18
F	0.73	0.50	0.90	0.44	0.76	0.88	0.85	0.49
Total	93.01	93.11	96.23	94.24	90.80	97.81	92.69	97.00

25 wt. % NaCl equivalent (Meinert 1992). Early hydrothermal fluids carrying large amount of dissolved salts exsolved from magma, and then a low-temperature and low-saline fluid was yielded probably through mixing with meteoric water (Meinert 1993).

The Galinge calc-alkaline granodiorite was closely related to the skarn mineralization. The common occurrence of halite-bearing fluid inclusions in anhedral quartz from the Galinge granodiorite suggests that high-saline and high-temperature hydrosaline fluids in the prograde stage were exsolved from the semi-solidified granodioritic magma at near solidus conditions. Inclusions in anhedral quartz from the Galinge granodiorite intrusions are classified into four types (Fig. 12), i.e., V (vapour phase), L (liquid phase), LHa (vapour phase + liquid phase + halite) and LHaSy (vapour phase + liquid phase + halite + sylvite) type (Wilkinson 2001; Yu et al. 2013b; Yu et al. 2014).

The Galinge granodiorite fluid inclusion microthermometry data are listed in Table 4 and summarized in Fig. 13. The salinity, density and minimum trapping pressure were calculated for the (simplified) NaCl-H_2O system (Roedder and Bodnar 1980; Bodnar and Vityk 1994). Homogenization temperature (Th) of inclusions in sample 2404-34 sample define three populations in the histogram (Fig. 13a), at: 240~360°C (peak value of 280°C); 380~460°C (peak value of 400°C); 500~560°C (peak value of 540°C). Salinity data also show three populations (Fig. 13b), at: 6~24 wt.% NaCl equiv. (peak value of 6 wt.% NaCl equiv.); 36~48 wt.% NaCl equiv. (peak value of 36 wt.% NaCl equiv.); 60~72 wt.% NaCl equiv. (peak value of 66 wt.% NaCl equiv.). Homogenization temperatures of inclusions in sample 2404-30range from 240°C to 340 °C (peak value of 300°C) (Fig. 13a), salinity data cluster around: 2~12 wt.% NaCl equiv. and 30~42 wt.% NaCl equiv. (Fig. 13b). Similar to sample 2404-30 the inclusions in sample 2404-36 have a significantly lower Th maximum of 280°C (range from 280°C to 340°C) (Fig. 13a) and a slightly lower salinity of 12~36 wt.% NaCl equiv. (Fig. 13b). Liquid phase inclusions in sample 26006-20 have Th ranging from 280 to 340°C (peak value of 280°C), and salinity ranging from 2~6 wt.% NaCl equiv. (Fig. 13b).

Discussion

Replacement of mafic igneous rocks

Mafic igneous rocks replaced by magmatic-hydrothermal fluids are reported in many skarn deposits (Einaudi and Burt 1982; Meinert 1984). There is a close link between igneous rock composition and skarn mineralogy. In general, skarn formed in volcanic rocks initially reflects the bulk composition of the protolith, but is later altered by the influx of metasomatic fluids.

Amphibole formation requires excessive amount of Si, Al, Fe, Mg, Ca, Na, K and Ti from the fluids and host rocks. Calcium, Na and K are likely to be the main constituents of magma derived hydrothermal fluid, as these elements are easily transported in saline solutions. Alteration of igneous protoliths to skarn assemblages generally results in a high concentration and strong mobility of elements such as Ti, V, and Al in calc-silicate minerals (Meinert 1984). For example, the breakdown of igneous feldspar can release Ca, Al, Na and K into the hydrothermal fluids. Therefore, Ca, Al, Na and K contents show an increasing trend from Amp-I to Amp-II. However, the common formation of magnesian-hastingsite, consuming substantial Al, K and Na, and later magma evolved fluid is characterized by low saline with relatively low K, Na and Ca content. Such factors may result in the depletion of Al,

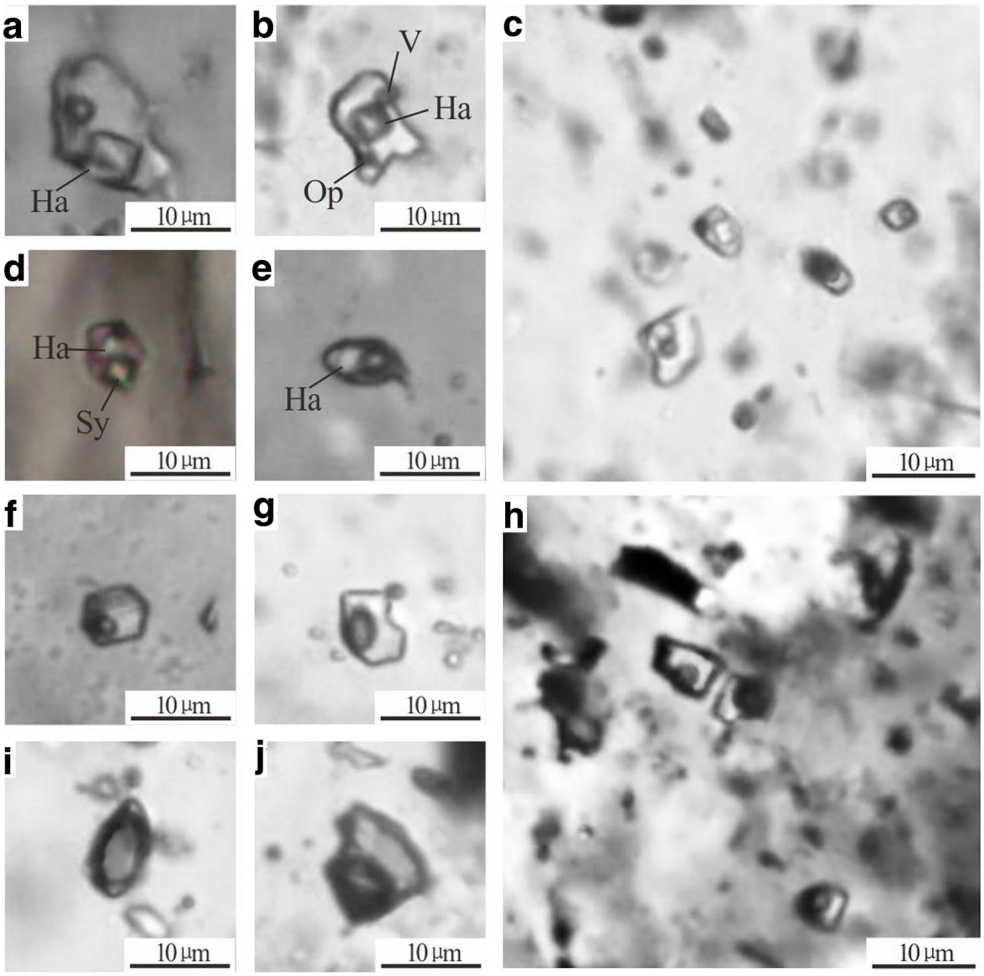

Fig. 12 Fluid inclusion (FI) photomicrographs of the Galinge granodiorite at room temperature under transmitted light. (**a**) 2404-34-22 LHa-type FIs containing ~20%vol spherical bubble, the cubic transparent daughter mineral is halite. (**b**) 2404-30-2 LHa-type FIs containing ~15%vol ellipsoidal bubble, a cubic transparent daughter mineral (halite) and a triangular opaque daughter mineral (possibly chalcopyrite). (**c**) 2404-30-1 V-type, L-type and LHa-type FIs coexisting in the same plane/cluster. (**d**) 2404-34-17 LHaSy-type FIs containing ~10%vol bubble and two cubic transparent daughter minerals (halite and sylvite). (**e**) 2404-34-24 LHa type FIs containing ~50%vol spherical bubble and cubic transparent halite. (**f**) 26006-20-5 negative crystal shape inclusion containing ~20%vol spherical bubble. (**g**) 2404-30-18 L-type FIs containing ~50%vol ellipsoidal bubble. (**h**) 26006-20-1 irregular inclusions in the altered granodiorite. (**i**) 2404-30-14 V-type vapor-rich FIs. (**j**) 2404-30-24 L-type FIs containing ~50%vol ellipsoidal bubble

K, Na and Ca from Amp-II to Amp-III, as illustrated in Figs. 9 and 10. In addition, the mole fraction of K in the A-site shows strong positive correlation with X_{Cl} for the Amp-II and Amp-III but very different slopes (Fig. 10), which indicates that they were probably formed under two distinct fluid environments. Amp-II may be associated with high saline fluid, but Amp-III may be yielded by low saline fluid. Nonetheless, Amp-I shows no obvious X_{Cl} and X_K correlation, implying that Amp-I was not generated by the replacement of hydrothermal fluids but most probably crystallized from the magmatic melt. The X_{Al} values from Amp-I to Amp-III shows a positive correlation with X_{Cl} values, indicating that the Al concentration of the octahedral site could influence the Cl incorporation.

Large amount of mafic Amp-II has extensively replaced the basaltic andesite rocks, showing that Fe and

Table 4 Summary of microthermometry data of fluid inclusions from the Galinge granodiorites

Sample	Mineral	Type	n	Tm_{halite} (°C)	ρ (g/cm3)	*pt* (Mpa)	wt% NaCl	Tm_{ice} (°C)	$Th_{L\text{-}V}$ (°C)
2404-30	qz	L	16		0.724~0.877	3.52~9.09	2.24~9.21	-6.0~-1.3	246~323
		LHa	3	245~317	1.048~1.100	2.95~9.25	34.37~37.19		245~329
		V	2		0.8	8.68	9.73	-6.4	285~318
2404-34	qz	L	14		0.77~0.92	6.04~10.95	9.08~20.07	-16.8~-5.9	242~344
		LHa	18	272~558	1.075~1.220	4.08~39.8	36.12~67.9		272~558
2404-36	qz	L	10		0.863~0.958	4.27~4.63	12.05~21.89	-19.3~-8.3	244~352
		LHa	2	158~164	1.066~1.068	2.98~3.0	29.98~30.22		240~244
26006-20	qz	L	12		0.685~0.77	6.74~13.03	4.03~4.65	-2.8~-1.0	281~335

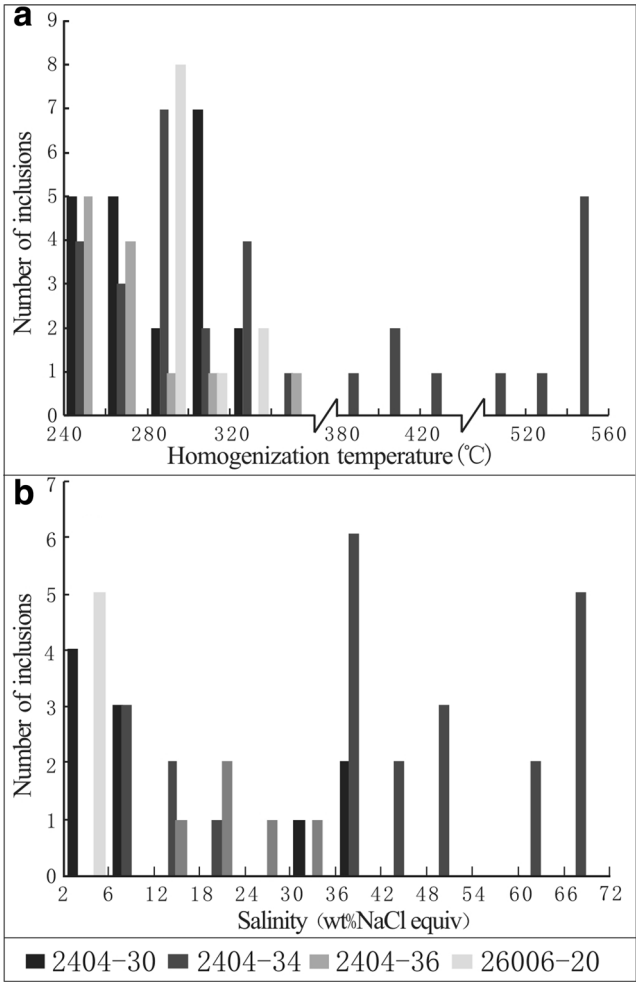

Fig. 13 Histogram showing homogenization temperatures and salinities of fluid-inclusion of all samples from Galinge granodiorite. **a**: Homogenization temperatures. **b**: Total Salinities (expressed as wt.% NaCl equiv.)

Mg were efficiently mobilized with the hydrothermal fluids. Compared with the Galinge dacite and rhyolite, the Galinge basaltic andesite has higher MgO and FeOt contents (Table 5). The extensively altered basaltic andesite contains lower MgO and FeOt contents than fresh one, which indicates that MgO and FeOt was likely to be mobilized by the hydrothermal leaching of basaltic andesite. Almost all X_{Mg} values from Amp-I to Amp-III are below 0.5 even though it has a wide range, but it is close to the average Mg# value (0.29) of fresh basaltic andesites. Furthermore, different amphibole generations show a wide range of Fe^{2+} and Mg concentrations likely reflecting the compositional variability of hydrothermal fluids and host rocks (Fig. 8).

The complete breakdown of primary plagioclase and the formation of Cl-rich amphibole indicate that a fluid phase was introduced along intergranular boundaries and microfractures throughout the fracture zones. Nevertheless, the large compositional variations of amphibole on the cm-scale suggest that the fluid flux was moderately low. This is supported by the incomplete breakdown of plagioclase along the ca. 3 cm wide metasomatism front (Fig. 3). Formation of magnesian hastingsite may have been associated with the decomposition of Amp-I and groundmass, since Mg and Fe content was preferentially incorporated into magnesian hastingsite. As there was no garnet formation at the metasomatic front, Amp-I and the groundmass of basaltic rocks may have supplied sufficient Ca for the Amp-II formation. Decomposition of feldspar can supply Ca and Si for the garnet formation in addition to Ca and Si in the fluid. A schematic reaction could be written as:

$$CaAl_2Si_2O_8(\text{anorthite}) + SiO_2(\text{quartz}) + 2CaCO_3(\text{calcite}) = Ca_3Al_2Si_3O_{12}(\text{grossular}) + 2CO_2$$

The narrow range of Ca for the three amphibole generations possibly reflects the restricted plagioclase composition (Fig. 8). The continuous introduction of fluid phase may have resulted in a system far diverted from the thermodynamic equilibrium.

Titanium from the Galinge fresh basaltic andesite rocks is dominantly hosted in sphene and intergrowths of ilmenite and titaniferous magnetite. When the ilmenite and titaniferous magnetite were dissolved later by volatile-rich hydrothermal fluids, titanium would be released into the hydrosaline fluids. The dissolved Ti would then be incorporated into sphene and titaniferous magnetite in the skarn rocks. The sphene grains in the skarn system developed a core-rim texture (Fig. 5), which suggests that the growth of sphene may have occurred in two stages. The early stage cores might be replacement relicts of the basaltic andesite during hydrothermal leaching process, and the second stage rims were probably formed during the skarn stage. The varying composition of the two stage sphenes reflects their hydrothermal fluid evolution.

Oxy-exsolution occurred in the high-Ti magnetite, forming exsolution lamellae of Fe-Ti oxides that are commonly present in most skarn deposits, and local pressure and fO_2 decrease is considered the most important cause for the oxy-exsolution of Fe-Ti-Al oxides in high-Ti magnetite (Hu et al. 2015). Solubility of Al and Ti is considered to be also strongly temperature dependent (Van Baalen 1993; Verlaguet et al. 2006), and is typically variable at sub-magmatic temperatures. Generally, higher Al and Ti contents in magnetite reflect a higher temperature in igneous systems (Nielsen et al. 1994). Therefore, Al and Ti incorporation in magnetite is largely temperature controlled (Nielsen et al. 1994; Toplis and Carroll 1995), and more likely to occur under high temperature

Table 5 Averaged chemical analyses (whole rock) of Galinge volcanic rocks

	Dacite (2) Average (%)	Rhyolite (5) Average (%)	Completely fresh andesite (6) Average (%)	Moderately altered andesite (2) Average (%)	Extensively altered andesite (2) Average (%)
SiO_2	68.5	74.67	59.51	58.3	55.55
Al_2O_3	15.37	12.21	16.27	15.55	16.12
FeOt	0.32	0.63	6.32	5.96	4.06
MgO	1.07	0.28	2.62	1.78	1.95
CaO	4.28	3.37	6.04	5.01	4.52
Na_2O	2.77	3.57	2.6	2.12	1.34
K_2O	4.22	1.27	2.87	2.23	1.66
TiO_2	0.35	0.08	0.75	0.64	0.87
P_2O_5	0.07	0.02	0.15	0.13	0.18
MnO	0.09	0.03	0.13	0.13	0.17
LOI	0.5	3.41	2.34	8.18	13.3
Total	97.51	99.55	99.6	100.02	99.71
$Mg^{\#}$	76.98	30.77	29.31	23.00	32.45
Average minor element contents (ppm)					
Zn	25.9	14.32	74.23	67.7	65.75
Cu	5.13	2.37	15.38	11.75	5.46
V	43.35	2.98	121	89.55	110.95
Pb	16.65	4.65	16.88	18.3	13.05
Co	5.06	2.78	17.15	12.7	11.1
Ti	1790	429	4228	4177.5	4115

igneous conditions. This thermodynamic principle is also applicable for hydrothermal magnetite (Nadoll et al. 2014). The Fe-Ti oxides geothermometer and oxygen barometer were calculated based on ILMAT (Lepage 2003) (Table 2 and Fig. 14). The computational temperature of hydrothermal magnetite ranges between 550°C and 700°C, and the oxygen fugacity varies between $10^{-14.74}$ and $10^{-17.94}$. The igneous titanomagnetite-ilmenite shows that crystallization temperature of volcanic rocks ranges from 700 to 750°C.

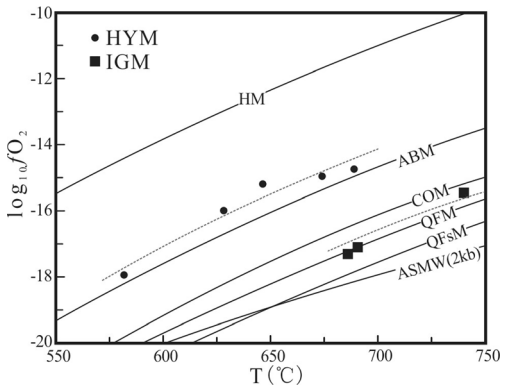

Fig. 14 Temperatures as oxygen fugacity of the Galinge Fe-Ti oxides (basemap after Frost and Lindsley (1992)). HYM: hydrothermal magnetite-ilmenite; IGM: igneous magnetite-ilmenite; HM: the hematite-magnetite oxygen buffer; ABM: the amphibole-biotite-magnetite oxygen buffer; QFM: quartz-fayalite-magnetite buffer; QFsM: quartz-ferrosilite-magnetite oxygen buffer; ASMW: annite-sanidine-magnetite-H_2O buffer under conditions of $P_{total} = P_{H_2O} = 2$ kbars; COM: augite-othopyroxene

Incorporation of Cl

In previous studies on Cl-rich amphibole, some factors for the substitution of OH by Cl in the amphibole structure have been introduced (Enami et al. 1992; Morrison 1991). Enami et al. (1992) argued that the Cl content of amphibole increases with increasing Cl concentration of the coexisting fluid in Cl-poor environments. Oberti et al. (1993) argued that the crystal-structure refinement of amphiboles shows strong compositional correlation with Cl incorporation. Furthermore, many studies of Cl-bearing amphiboles emphasized the positive correlations of X_{Al} and X_K with X_{Cl} (Fig. 10), which suggests that the Cl content is interrelated with A-site occupancy. (Morrison 1991; Suwa et al. 1987; Vanko 1986). Sato et al. (1997) pointed out that the incorporation of Cl in amphibole is governed by crystal chemical constraints. Substitution of Cl for OH expands the size of the octahedral sites (Makino et al. 1993), and Al substitution for Si could cause the deformation of double chains to fit the expanded octahedral strips. The effects of Fe substitution into octahedral sites on the Cl incorporation may be a chemical one (Vanko 1986).

Munoz and Swenson (1981) and Morrison (1991) have suggested that the Cl-OH exchange reaction between amphibole and a coexisting fluid or silicate melt can be modeled as follows:

$$OH_{amp} + Cl_{fluid\ or\ melt} = Cl_{amp} + OH_{fluid\ or\ melt} \quad (1)$$

The equilibrium constant (K) for this reaction can be given as:

$$\log K = \log(Cl/OH)_{amp} - \log(Cl/OH)_{fluid\ or\ melt} \quad (2)$$

The Cl distribution may be ideally expressed:

$$\ln(Cl/OH)_{amp} = \ln(Cl/OH)_{fluid} - \Delta G^0/RT \quad (3)$$

where ΔG^0 is the free energy change of the end-members in reaction (1), R and T are ideal gas constant and temperature, respectively. Obviously, the ΔG^0 varies with the cation contents in amphibole. Since $^{[4]}Al$ and Fe^{2+} exert the principal compositional control on Cl incorporation, the ΔG^0 may be related with the product of the $^{[4]}Al$ and Fe^{2+} content. Moreover Sato et al. (1997) pointed out that the temperature and composition are related with ΔG^0. Therefore, the equation (3) may be written as (Sato et al. 1997):

$$\ln(Cl/OH)_{amp} = \ln(Cl/OH)_{fluid} + A \cdot {}^{[4]}Al \cdot Fe^{2+}/RT + B/RT \quad (4)$$

If T and $\ln(Cl/OH)_{fluid}$ values are given, amphiboles with variable $\ln(Cl/OH)_{amp}$ should be a linear function of $^{[4]}Al \cdot Fe^{2+}$. Thus, the three distinct trends in the $^{[4]}Al \cdot Fe^{2+}$ vs. ln(Cl/OH) plots (Fig. 15) for the three generations amphiboles (FE, MH and FA) probably indicate that the replacement and growth of amphiboles took place under variable physical-chemical conditions of the coexisting hydrothermal fluids (Sato et al. 1997). They also reflect the $\ln(Cl/OH)_{fluid}$ values

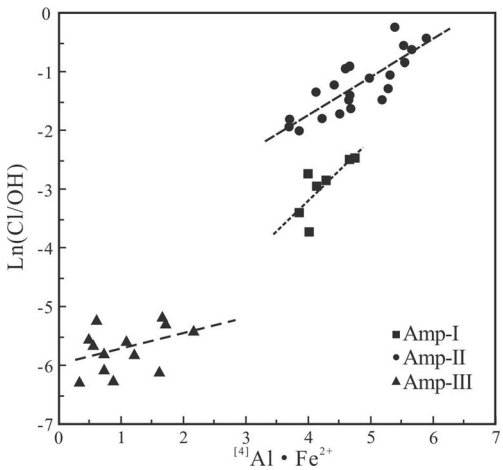

Fig. 15 $^{[4]}Al \cdot Fe^{2+}$ vs. ln(Cl/OH) diagram for Amp-I, Amp-II and Amp-III from the Galinge deposit

of the MH-forming fluids were higher than the ones of the FA-forming fluid. Therefore, the Cl concentrations of MH-forming fluids are higher than the ones forming the FA. As a consequence, the formation of MH might be associated with the early high-temperature and higher saline fluid, whereas the FA formed from later low-temperature and low-saline fluids.

Implications of fluid inclusions

Studies of various skarn systems have revealed that the magmatic fluid evolution is a dominant factor for the formation of diverse skarn mineral assemblages. At Galinge hydrothermal events are divided into two major stages, as in many skarn deposits worldwide (Meinert et al. 2003; Öztürk et al. 2008). Early high-temperature and high-saline fluids exsolved from semi-solidified magma carrying large amounts of dissolved salts, followed by a later stage of low-temperature and low-saline fluids generated probably through meteoric water influx (Fig. 13). The halite-bearing inclusions coexisting with the vapor-rich inclusions are considered to be the consequence of phase separation at largely constant pressure and temperature, which can be taken as an evidence for immiscibility or boiling (Hemley et al. 1992; Wilkinson 2001). Fluid immiscibility, especially emanation of volatiles and changes in pH and oxidation state, have become well appreciated with regard to the ore-forming processes.

At early prograde stage anhydrous minerals, such as garnet and clinopyroxene, formed from relatively high-temperature and high-saline fluids; during the later retrograde stage with hydrous minerals, such as epidote, amphibole, and chlorite plus sulfide ore minerals form from low-temperature and low-saline fluids. Accordingly the Cl-rich MH documented in this study was formed coeval with the garnet. It formed by the replacement of original igneous FE through the early high-temperature and high-saline hydrothermal fluid. The formation of Cl-poor FA would be associated with the later low-temperature and low-saline fluid alteration. The differences in Cl content among the amphiboles may reflect equilibration at significantly different temperatures and broadly varying fluid salinity (Morrison 1991; Sato et al. 1997). We suggest that, during an early hydrothermal event, a relatively high-temperature and high-saline fluid altered the original FE to the Cl-rich MH at the crystal margins adjacent to circulating fluids. Late-stage hydrothermal alteration by a low Cl content and low-temperature fluid produced FA at the rims of grains.

The segregation and release of a fluid phase from the crystallizing melt are of particular importance to skarn formation (Meinert 1993). The H_2O solubility in silicate melts saturated in aqueous vapor and/or hydrosaline liquid varies inversely with Cl^- content. The presence of a magmatic volatile phase buffers the H_2O and Cl^- concentrations of the silicate melt. Hydrosaline liquids are stable with higher Cl contents in the melt, and H_2O solubility is highly sensitive to Cl content.

Thus, Cl is much more likely to affect the exsolution of hydrosaline liquid vapor from highly-evolved, H_2O-poor, silicic melts because these melts saturate in these phases if they contain as little as several thousand ppm Cl (Webster and Rebbert 1998). Since the solubility of Cl^- in silicic melts is much lower than in mafic melts (Webster 1997), large amounts of Cl^- would be exsolved from magmas along with fractional crystallization (Webster et al. 1999).

Concluding remarks

Multistage amphiboles in iron skarn deposits are rarely reported. Amphiboles from the Galinge skarn deposit are compositionally and paragenetically divided into three generations: Amp-I: Ferro-edenitic hornblende (FE); Amp-II: Deep bluish-green magnesian-hastingsite (MH); Amp-III: Light greenish-beige ferro-actinolite (FA). Both Mg and Fe contents of the MH and FA vary widely, which may reflect the interactions between magmatic-derived hydrothermal fluids and the basaltic andesite host rock.

Mineralogical studies on multistage amphiboles provide insights into the formation mechanisms that control Cl incorporation into the OH site. Our work confirms that the varying Cl content in amphiboles is controlled by temperature and the quite variable salinity of the hydrothermal fluids. In prograde alteration stage, high-temperature and high-saline fluids exsolved from the granodioritic magma, have replaced the primary FE in the mafic igneous rocks to form the Cl-rich MH, and was succeeded by formation of the Cl-poor FA during retrograde alteration (low-temperature and low-saline fluids). The Cl-rich fluids could concentrate some elements such as Fe, Cu, and Ca etc. in the solution and transport them as metal chloride complexes.

Acknowledgments This study was jointly financially supported by the National Natural Science Foundation of China (Grant 41172076), the Program of High-level Geological Talents (201309) and Youth Geological Talents (201112) of the China Geological Survey, Geological Survey Program (Grant 1212011085528) from the China Geological Survey, and the Scientific Research Fund (Grant 201411025) of the Non-Commercial Unit from Ministry of Land and Resources, China.

Thanks are due to the Editor-in-Chief Johann G. Raith and Associate Editor Georg Hoinkes for editorial handling, and to the two reviewers for their constructive and thoughtful comments. Cenozoic Geoscience Editing is acknowledged for their language polishing and scientific editing services.

References

Baker J, Spiegelman M (1995) Modelling an infiltration-driven geochemical front. Earth Planet Sc Lett 136:87–96

Bally AW (1986) Notes on sedimentary basins in China: report of the American sedimentary basins delegation to the People's Republic of China. Department of the Interior, US Geological Survey, 86-327

Bodnar RJ, Vityk MO (1994) Interpretation of microthermometric data for H_2O-NaCl fluid inclusions. Fluid Inclusions in Minerals: Methods and Applications:117–130

Dick LA, Robinson GW (1979) Chlorine-bearing potassian hastingsite from a sphalerite skarn in southern Yukon. Can Mineral 17:25–26

Duke EF (1995) Contrasting scales of element mobility in metamorphic rocks near Harney Peak Granite, Black Hills, South Dakota. Geol Soc Am Bull 107:274–285

Dutrow BL, Foster CT, Henry DJ (1999) Tourmaline-rich pseudomorphs in sillimanite zone metapetites: Demarcation of an infiltration front. Am Mineral 84:794–805

Einaudi MT, Burt DM (1982) Introduction; terminology, classification, and composition of skarn deposits. Econ Geol 77:745–754

Enami M, Liou JG, Bird DK (1992) Cl-bearing amphibole in the Salton Sea geothermal system, California. Can Mineral 30:1077–1092

Feng CY, Li DS, Wu ZS, Li JH, Zhang ZY, Zhang AK, Shu XF, Su SS (2010) Major types, time-space distribution and metallogenesis of polymetallic deposits in the Qimantage metallogenic belt, eastern Kunlun area. Northwest Geol 43:10–17

Feng CY, Zhao YM, Li DX, Liu JN, Xiao Y, Li GC, Ma SC (2011) Skarn types and mineralogical characteristics of the Fe-Cu-polymetallic skarn deposits in the Qimantage area, Western Qinghai Province. Acta Geol Sin 85:1108–1115

Feng CY, Wang S, Li GC, Ma SC, Li DS (2012) Middle to Late Triassic granitoids in the Qimantage area, Qinghai Province, China: Chronology, geochemistry and metallogenic significances. Acta Petrol Sin 28:665–678

Frost BR, Lindsley DH (1992) Equilibria among Fe-Ti oxides, pyroxenes, olivine, and quartz: Part II. Application Am Mineral 77:1004

Grigsby JD (1990) Detrital magnetite as a provenance indicator. J Sediment Res 60:940–951

Hawthorne FC, Oberti R (2006) On the classification of amphiboles. Can Mineral 44:1–21

Hawthorne FC, Oberti R, Harlow GE, Maresch WV, Martin RF, Schumacher JC, Welch MD (2012) Nomenclature of the amphibole supergroup. Am Mineral 97:2031–2048

Hemley JJ, Cygan GL, Fein JB, Robinson GR, D'Angelo WM (1992) Hydrothermal ore-forming processes in the light of studies in rock-buffered systems; I, Iron-copper-zinc-lead sulfide solubility relations. Econ Geol 87:1–22

Hu H, Lentz D, Li J, Mccarron T, Zhao X, Hall D (2015) Reequilibration processes in magnetite from iron skarn deposits. Econ Geol 110:1–8

Jacobson SS (1975) Dashkesanite: high-chlorine amphibole from St. Paul's rocks, Equatorial Atlantic and Transcaucasia, USSR. Smithson. Contrib. Earth Sci 14:17–20

Krutov GA (1936) Dashkesanite, a new chlorine amphibole of the hastingsite group. Mineral Abstr 6:438

Leake BE (1978) Nomenclature of amphiboles. Can Mineral 16:501–520

Leake BE, Woolley AR, Arps C, Birch WD, Gilbert MC, Grice JD, Hawthorne E, Kato A, Kisch HJ, Krivovichev VG (1997) Nomenclature of amphiboles report of the subcommittee on amphiboles of the International Mineralogical Association Commission on new minerals and mineral Names. Eur J Mineral 61:295–361

Leake BE, Woolley AR, Birch WD, Burke EA, Ferraris G, Grice JD, Hawthorne FC, Kisch HJ, Krivovichev VG, Schumacher JC (2004) Nomenclature of amphiboles: Additions and revisions to the International Mineralogical Association's amphibole nomenclature. Am Mineral 89:883–887

Lepage LD (2003) ILMAT: an Excel worksheet for ilmenite–magnetite geothermometry and geobarometry. Comput Geosci 29:673–678

Li GM, Shen YC, Liu TB (2001) Geological and geochemical characteristics of Variscan granite in the Qimantage Region, Eastern Kunlun. Geophys Prospect 1:16

Luo ZH, Deng JF, Cao YQ, Guo ZF, Mo XX (1999) On late Paleozoic-early Mesozoic volcanism and regional tectonic evolution of Eastern Kunlun, Qinghai Province. Geoscience 13:51–56

Luo ZH, Ke S, Cao YQ, Deng JF, Zhan HW (2002) Late Indosinian mantle-derived magmatism in the East Kunlun. Geol Bulletin China 21:292–297

Makino K, Tomita K, Suwa K (1993) Effect of chlorine on the crystal structure of a chlorine-rich hastingsite. Mineral Mag 57:677–686

Mao JW, Zhou ZH, Feng CY, Wang Y, Zhang C, Peng H, Miao Y (2012) A preliminary study of the Triassic large-scale mineralization in China and its geodynamic setting. Geol China 39:1437–1471

Meinert LD (1984) Mineralogy and petrology of iron skarns in western British Columbia, Canada. Econ Geol 79:869–882

Meinert LD (1992) Skarns and skarn deposits. Geosci Can 19:145–162

Meinert LD (1993) Igneous petrogenesis and skarn deposits. Mineral deposit modeling 40:569–583

Meinert LD, Hedenquist JW, Satoh H, Matsuhisa Y (2003) Formation of anhydrous and hydrous skarn in Cu-Au ore deposits by magmatic fluids. Econ Geol 98:147–156

Morrison J (1991) Compositional constraints on the incorporation of Cl into amphiboles. Am Mineral 76:1920–1930

Munoz JL, Swenson A (1981) Chloride-hydroxyl exchange in biotite and estimation of relative HCl/HF activities in hydrothermal fluids. Econ Geol 76:2212–2221

Nadoll P, Angerer T, Mauk JL, French D, Walshe J (2014) The chemistry of hydrothermal magnetite: a review. Ore Geol Rev 61:1–32

Nielsen RL, Forsythe LM, Gallahan WE, Fisk MR (1994) Major-and trace-element magnetite-melt equilibria. Chem Geol 117:167–191

Oberti R, Ungaretti L, Cannillo E, Hawthorne FC (1993) The mechanism of Cl incorporation in amphibole. Am Mineral 78:746–752

Öztürk YY, Helvacı C, Satır M (2008) The influence of meteoric water on skarn formation and late-stage hydrothermal alteration at the Evciler skarn occurrences, Kazdağ, NW Turkey. Ore Geol Rev 34:271–284

Roedder E, Bodnar RJ (1980) Geologic pressure determinations from fluid inclusion studies. Annu Rev Earth Pl Sc 8:263

Sato H, Yamaguchi Y, Makino K (1997) Cl incorporation into successively zoned amphiboles from the Ramnes cauldron, Norway. Am Mineral 82:316–324

Suwa K, Enami M, Horiuchi T (1987) Chlorine-rich potassium hastingsite from West Ongul island, Liitzow-Holm bay, East Antarctica. Mineral Mag 51:709–714

Toplis MJ, Carroll MR (1995) An experimental study of the influence of oxygen fugacity on Fe-Ti oxide stability, phase relations, and mineral-melt equilibria in ferro-basaltic systems. J Petrol 36:1137–1170

Van Baalen MR (1993) Titanium mobility in metamorphic systems: a review. Chem Geol 110:233–249

Vanko DA (1986) High-chlorine amphiboles from oceanic rocks: product of highly saline hydrothermal fluids. Am Mineral 71:51–59

Verlaguet A, Brunet F, Goffé B, Murphy WM (2006) Experimental study and modeling of fluid reaction paths in the quartz - kyanite ± muscovite - water system at 0.7 GPa in the 350–550°C range: implications for Al selective transfer during metamorphism. Geochim Cosmochim Ac 70:1772–1788

Wang BZ, Luo ZH, Li HY, Shen HW, Hu XL (2009) Petrotectonic assemblages and temporal-spatial framework of the Late Paleozoic-Early Mesozoic intrusions in the Qimantage Corridor of the East Kunlun belt. Geol China 36:769–782

Webster JD (1997) Exsolution of magmatic volatile phases from Cl-enriched mineralizing granitic magmas and implications for ore metal transport. Geochim Cosmochim Ac 61:1017–1029

Webster JD, Rebbert CR (1998) Experimental investigation of H_2O and Cl^- solubilities in F-enriched silicate liquids; implications for volatile saturation of topaz rhyolite magmas. Contrib Mineral Petrol 132: 198–207

Webster JD, Kinzler RJ, Mathez EA (1999) Chloride and water solubility in basalt and andesite melts and implications for magmatic degassing. Geochim Cosmochim Ac 63:729–738

Wilkinson JJ (2001) Fluid inclusions in hydrothermal ore deposits. Lithos 55:229–272

Wu YZ, Qiao GB, Chen DH (2011) A preliminary study on relationship between tectonic magmatism and mineralization in Qimantage area, Eastern Kunlun Mountains. Geotecton Metallog 35:232–241

Xu ZQ, Yang JS, Li WC, Li HQ, Cai ZH, Yan Z, Ma CQ (2013) Paleo-Tethys system and accretionary orogen in the Tibet Plateau. Acta Petrol Sin 29:1847–1860

Yu M (2013) Geochemistry and zonation of the Galinge iron deposit, Qinghai province. China University of Geoscience, Bejing, p 1–106

Yu M, Feng CY, Bao GY, Liu HC, Zhao YM, Li DX, Xiao Y, Liu JN (2013a) Characteristics and zonation of skarn minerals in Galinge iron deposit, Qinghai Province. Mineral Deposits 32:55–76

Yu M, Feng CY, Xiao Y, Liu JN, Li DX, Li GC, Ma SC (2013b) Features and evolution of metallogenic fluid in Jiadanggen porphyry copper deposit of Gonghe Country, Qinghai Province. Mineral Deposits 32: 133–147

Yu M, Feng CY, Zhao YM, Li DX, Xiao Y, Liu JN, Li ZF (2014) Fluid inclusion geochemistry in the Kaerqueka copper polymetallic deposit, Qinghai Province and its genetic significances. Acta Geol Sini 88:903–917

Yu M, Feng CY, Liu HC, Li DW, Zhao Y, Li DX, Liu JN, Wang H, Zhang MH (2015a) ^{40}Ar-^{39}Ar geochronology of the Galinge large skarn iron deposit in Qinghai province and geological significance. Acta Geol Sini 89:510–521

Yu M, Feng CY, Zhao YM, Li DX (2015b) Genesis of post-collisional calc-alkaline and alkaline granitoids in Qiman Tagh, East Kunlun, China. Lithos 239:45–59

Zhang JX, Meng FC, Wan YS, Yang JS, Dong GA (2003) Early Paleozoic tectono-thermal event of the Jinshuikou Group on the southern margin of Qaidam: Zircon U-Pb SHRIMP age evidence. Geol Bulletin China 22:397–404

Zhao YM, Feng CY, Li DX, Liu JN, Xiao Y, Yu M, Ma SC (2013) Metallogenic setting and mineralization-alteration characteristics of major skarn Fe-polymetallic deposits in Qimantag area, western Qinghai Province. Mineral Deposits 32:1–19